Desalination and Water Treatment
www.deswater.com

doi: 10.1080/19443994.2016.1175772

57 (2016) 27587–27600
December

Taylor & Francis
Taylor & Francis Group

Developing statistical models for estimating *chlorophyll-a* and total suspended solid levels at an estuarine reservoir with nutrient inputs from satellite observations

Seo Jin Ki[a,1], Jihwan Park[b,1], Yongeun Park[c], Dong Jin Jeon[a], Joon Ha Kim[a,*]

[a]*School of Environmental Science and Engineering, Gwangju Institute of Science and Technology (GIST), Gwangju 61005, Republic of Korea, email: joonkim@gist.ac.kr (J.H. Kim)*
[b]*Research and Development Group, Korea Electronics Recycling Cooperative (KERC), Gangnamdae-ro 262, Gangnam-gu, Seoul 06265, Republic of Korea*
[c]*Environmental Microbial & Food Safety Laboratory, USDA-ARS, 10300 Baltimore Ave., Beltsville, MD 20705, USA*

Received 15 February 2016; Accepted 5 April 2016

ABSTRACT

Providing high-resolution monitoring data is essential in promoting decision-making activities for surface water quality protection such as scientific modeling and data analysis. In this study, statistical models using multiple linear regression (MLR) were developed to estimate *Chlorophyll-a* (Chl-a) and total suspended solid (TSS) concentrations in a mesotrophic reservoir, the Yeongam Reservoir in Korea, from satellite observations. Two types of satellite data that covered different spectral regions, for wavelengths in 412–865 nm (for the Geostationary Ocean Color Imager) and those in 405–14,385 nm (for the Moderate Resolution Imaging Spectroradiometer), were used as inputs for statistical models, after bias correction. The MLR models for Chl-a and TSS were initially constructed and evaluated with 39 image data-sets obtained during 2011–2014. Subsequently, they compared with their corresponding algorithms that were developed under different environmental settings as well as the CE-QUAL-W2 model, a numerical model of reservoir water quality. Sensitivity analysis showed that specific red and near-infrared wavelengths significantly contributed to improve the accuracy of the Chl-a and TSS estimates, respectively, along with those of blue and green bands typically used. The constructed MLR models showed better performance than the simulation model as well as the classical and recent bio-optical algorithms on average. In particular, poor prediction performance for total nitrogen and total phosphorus caused by a lack of adequate input data and description of transport mechanisms appeared to lower the accuracy of the Chl-a and TSS estimates in the simulation model. Therefore, these results demonstrate that statistical models developed from satellite observations can be used to rapidly screen local water quality and to provide high-quality data for reservoir water quality management.

*Corresponding author.

[1]These two authors contributed equally to this work.

1944-3994/1944-3986 © 2016 Balaban Desalination Publications. All rights reserved.

Keywords: Bio-optical algorithms; Geostationary Ocean Color Imager; Moderate Resolution Imaging Spectroradiometer; Multiple linear regression; CE-QUAL-W2 model; Reservoir water quality

1. Introduction

Excessive nutrient inputs from anthropogenic activities have caused eutrophication of aquatic ecosystems [1], with episodes of contamination in global water resources such as nuisance and harmful algae blooms (HABs) [2–4]. *Chlorophyll-a* (Chl-a) and total suspended solid (TSS) concentrations were considered as primary parameters for providing the early prediction of algal blooms as well as diagnosing the eutrophication status of surface water systems [5–7]. Measurements of the hydrologic and water quality characteristics including Chl-a and TSS in a regular monitoring program, however, were performed at low spatial and temporal resolutions due to financial and time constraints, e.g. only from three monitoring locations on a monthly basis at best for large reservoir systems in Korea [8]. To address the limitations arising from sparse monitoring data in space and time, the use of remote-sensing data is now favored and materialized as a promising technique for illustrating water quality conditions, or even developing alternative statistical models based on these profiles.

To estimate water quality constituent concentrations from satellite observations, the previous studies suggested a methodology that derived the remote-sensing reflectance from the inherent optical properties (IOPs) of water bodies [9]. The underlying assumptions in this approach are that the optical properties of phytoplankton pigments and detrital particles are mainly responsible for characterizing the Chl-a levels, whereas those of miscellaneous particles including both algal and non-algal components are related to the TSS concentrations. This analytical approach, referred as a bio-optical model, was initially tested in feasibility studies to calculate the Chl-a and TSS profiles in ocean surface waters [10–12]. Subsequently, it provided the basis for the development of semi-analytical methods (e.g. the Garver, Siegel, and Maritorena Model (GSM), and Quasi-Analytical Algorithm (QAA) models) which reflected multiple ocean properties [13,14].

In these models, a band ratio was often used to calculate the Chl-a concentrations in optically deep waters (namely CASE-1 water) by assuming that the optical properties of phytoplankton exhibited the maximum and minimum absorption in blue and green wavelengths [5,15,16]. The OC4v.4 and OC3 M models were the bio-optical algorithms which were developed for Chl-a using the ratio of green and blue band reflectance in the Sea-Viewing Wide Field-of-View Sensor (SeaWiFS) and Moderate Resolution Imaging Spectroradiometer (MODIS) images, respectively [16]. The earlier models derived empirically were, however, less successful in providing the Chl-a profiles at more optically complex waters (namely CASE-2 water) which contained the elevated levels of colored dissolved organic matter and other minor contaminants [17–20]. As an alternative to the existing bio-optical algorithms, the Near-Infrared (NIR)-red models that used multiple wavebands in NIR and red regions were recently developed to estimate the Chl-a levels in turbid waters [20–22]. Two-band NIR-red model included one wavelength ranging between 660 and 690 nm (in the red region) and the other ranging between 700 and 730 nm (in the NIR region), whereas one additional wavelength that was greater than the 730 nm was incorporated into three-band NIR-red model. Note that all these wavelengths are found to be minimally affected by any constituents in the complex water columns [17–24].

The conventional band ratio algorithms including the Clark's model were also used to estimate the TSS concentrations in open water regions (i.e. CASE-1 water). Those algorithms were developed specifically using the band ratio ranging from 440 to 550 nm [25], but still did not show good performance in CASE-2 water, as shown in the Chl-a estimation [26,27]. Accordingly, the recent studies recommended the development of new bio-optical algorithms for CASE-2 water using single or multiple bands, including the band ratio, from different satellite images. Currently, various algorithms which reflect the spectral idiosyncrasy of individual waters are tested to help researchers quantify the TSS levels under site-specific variability in their optical properties [28–30].

The objectives of this study are to determine particular spectral bands which play an important role in estimating both Chl-a and TSS profiles, and then to develop multiple linear regression (MLR) models using these bands as predictor variables. This is because the site-specific models are probably more suitable for quantifying the constituent levels in local estuarine waters (with sporadic nutrient inputs from interconnected water system) than the conventional

models that are developed and examined in different environmental settings. Thus, the significance of this study can be described in terms of three aspects. First, a sensitivity analysis was conducted to rank the spectral bands in order of importance available in both 1-km MODIS and 500-m Geostationary Ocean Color Imager (GOCI) images. Note that the bands selected from this process for use in the MLR models for Chl-a and TSS may be different from those that were historically used in literature. Second, a comparison was made between the MLR models and their corresponding bio-optical algorithms such as the conventional (OC4v.4, OC3 M, GDPS standard, and Clark's models), NIR-red models, etc. This will ensure the suitability of the MLR models which are developed from either of two images for estimating the Chl-a and TSS levels in local waters. Finally, the performance of the MLR models was compared against the CE-QUAL-W2 model, a two-dimensional reservoir water quality model (i.e. the US Army Corps of Engineers in USA), to assess their accuracy and usefulness in rapidly screening estuarine water quality conditions [31–34].

2. Materials and methods

2.1. Study area

The study area of the Yeongam Reservoir (YAR), constructed in 1993, is located in the southwestern part of the Korean peninsula facing the Yellow sea (see Fig. 1). As an interconnected reservoir system, the YAR is located midway between the Yeongsan Reservoir (YSR) and Kumho Reservoir. The YAR had a surface area of 42.9 km^2 with average annual storage capacity of 280 million tons per year, according to the historical records of reservoir operation in 2011–2013. The intended purposes of the combined reservoir system were to provide stable supply of irrigation water and to improve flood protection for surrounding land areas reclaimed along these estuarine reservoirs [35]. The YAR received most of water resources including nutrient inputs through an artificial open channel from the YSR that was considered as the most heavily polluted waterway among the four major rivers in South Korea [36]. Due to this reason, the YAR was routinely classified as a mesotrophic reservoir [37]. The annual average Chl-a and TSS concentrations recorded in 1993 were 13.77 mg/m^3 and 15.86 mg/L, respectively.

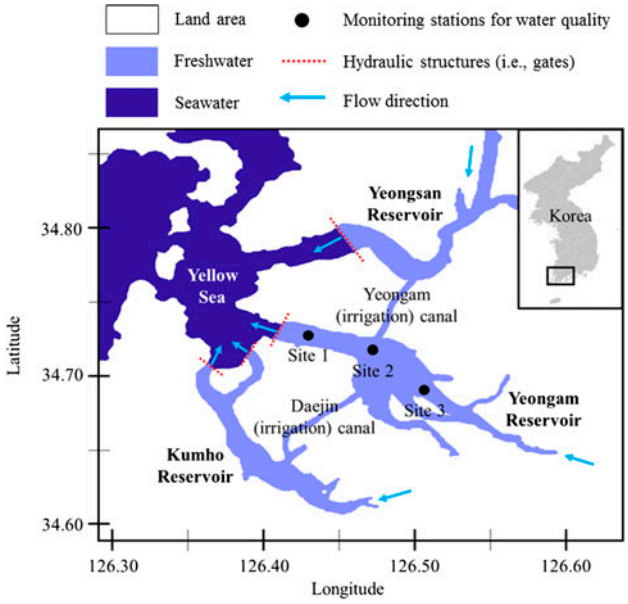

Fig. 1. A core area of study at the YAR and the interconnected reservoirs, the YSR and Kumho Reservoir, located in the southwestern part of Korea. Three solid circles indicate the monitoring sites in the target reservoir.

2.2. Environmental monitoring data acquisition for the YAR

Water quality data were obtained from the Yeongsan River Environment Research Center supervised by the National Institute of Environmental Research in Korea (http://water.nier.go.kr/waterMeasurement/selectWater.do). The physical, biological, and chemical water quality characteristics were measured monthly at three sampling sites in the YAR (see Fig. 1) where the data from Jan 2011 to Dec 2014 were specifically compiled. In each sample point, multiple depths in the water column were measured, i.e. at the surface (0.5 m), mid-depth (8 m), and near-bottom (17 m). However, the Chl-a and TSS levels observed in the surface layer were only used for a comparison with their corresponding values estimated by the MLR models that were derived from GOCI and MODIS, respectively. Daily meteorological data in the Mokpo City station adjacent to the YAR during a 2-year period (2011–2012) were collected from the Korea Meteorological Administration. These data included the temperature, dew point, precipitation, solar intensity, wind speed, wind direction, and cloud cover percentage. Hydrologic data of the YAR (i.e. the daily inflow rate, outflow rate, and gate operation) were also provided by the Korea Rural Community and Agricultural Corporation during the same period. Both meteorological and hydrologic data, once compiled, were then used to establish the boundary and initial conditions of the CE-QUAL-W2 model, along with the water quality profiles in other layers, i.e. mid-depth and near-bottom.

2.3. Data acquisition and processing for satellite images

A methodology that derived the remote-sensing reflectance, $R_{rs}(\lambda)$, from the IOPs of water bodies was proposed by Gordon et al. [9], such that

$$R_{rs}(\lambda) \approx \frac{b_b(\lambda)}{a(\lambda) + b_b(\lambda)}\gamma \quad (1)$$

where $a(\lambda)$, $b_b(\lambda)$, and γ indicate the absorption coefficient at wavelength λ, the backscattering coefficient, and the parameter that is related to the volume scattering function defined depending on the geometry of light emerging from the water surface, respectively [10,11].

For this study, two satellite observations, the level-1B GOCI and MODIS images, were obtained for 13 d in 2011–2014 from the websites maintained by the Korea Ocean Satellite Center (http://kosc.kiost.ac/kosc_web/GOCI_download/SatelliteData.html) and National Aeronautics and Space Administration (NASA) Goddard Space Flight Center (http://ladsweb.nascom.nasa.gov/data/), respectively. For data consistency between satellite and field observations, the satellite images which were within a three-hour time difference with the field water quality measurements were selected only [12,38]. Also, when three GOCI images between 10:30 and 12:30 in local time were collected, one image from the Terra MODIS sensor was collected in the morning to match the sampling time between the images. Both satellite data were then divided into two groups, the initial data-set for developing the MLR models (2011–2012) and remaining data-set for evaluating their applicability in local waters (2013–2014).

Note that during the satellite image processing, an atmospheric correction was applied to the level-1B data from the GOCI and MODIS. This is because the water-leaving radiance (L_w) was typically affected by the absorption and scattering interference as well as the cloud masking [28,39]. For this study, the modified North Sea Mathematical Models algorithm was used to adjust atmospheric disturbances in the satellite observations [40–42]. This was specifically performed using the Environment for Visualizing Images (version 4.5, Research Systems Inc., Colorado) and SeaWiFS Data Analysis System (version 7.0.1, Ocean Biology Processing Group, NASA Goddard Space Flight Center, Maryland) tools for the GOCI and MODIS images, respectively. Once atmospheric corrections were completed, a 3×3 box test was examined to confirm the homogeneity of reflectance at a reference pixel. This test was conducted by comparing the reference pixel and its surrounding pixels to avoid a wrong choice of the pixel affected by the patchy water [19,43]. Table 1 shows the Chl-a and TSS levels at three sampling sites in the YAR for 14 different dates, which are converted from 39 GOCI images through a series of image processing operations, as discussed above.

2.4. MLR model

2.4.1. Selection of model parameters

Determining predictor variables that are responsible for changes in the Chl-a and TSS levels at local waters may play an important role in constructing statistical models. In this study, the sensitivity analysis was performed using the Latin Hypercube One factor At a Time (LH-OAT) technique that evaluated the effect of individual parameters on model outputs. The LH-OAT method, frequently used in hydrologic and watershed models, refers to a technique that combines the Latin Hypercube (LH) sampling and One-Factor-At-a-Time (OAT) design, as its name implies. As an extension form of the Monte Carlo random sampling [44], the method is specifically more powerful than random (or too spare) and full factorial (or too dense) samplings in terms of computational efficiency. In this analysis, the partial effect for each parameter changed is calculated by repeatedly moving the initial LH points to other positions as follows:

$$S_{i,j} = \left| \frac{100 \times \left\{ \frac{M(e_1,\ldots,e_i\cdot(1+g_i),\ldots,e_p) - M(e_1,\ldots,e_i,\ldots,e_p)}{[M(e_1,\ldots,e_i\cdot(1+g_i),\ldots,e_p) + M(e_1,\ldots,e_i,\ldots,e_p)]/2} \right\}}{g_i} \right| \quad (2)$$

where $S_{i,j}$ is the partial sensitivity for a parameter e_i, M is the model function, g_i is the fraction by which a parameter e_i is changed, and j refers to the LH points. From this calculation, four highly ranked bands which were most sensitive to the model outputs were selected for developing the MLR models for Chl-a and TSS (see Table 2), regardless of the spectral bands that were historically preferred in literature [45]. More detailed information on the LH-OAT method is available elsewhere [46,47].

2.4.2. MLR model construction

In this study, four MLR models were developed individually according to the satellite types (GOCI: G and MODIS: M) and dependent variables (i.e. Chl-a and TSS), hereafter referred to as MLR(G)-Chl-a, MLR(G)-TSS, MLR(M)-Chl-a, and MLR(M)-TSS (see Table 2). The coefficients of independent variables in the MLR models were using SPSS Statistics (version 17.0, SPSS

Table 1
The Chl-a and TSS levels at three sampling sites in the YAR for 14 different dates which are converted from the GOCI images through image processing operations. The precipitation and inflow records present input data to the CE-QUAL-W2 model[a]

Dates	Sites	TSS levels (mg/L)	Chl-a levels (mg/m^3)	Precipitation (mm)	Inflow (m^3)
12 April 2011	1	6.4	10.1	$^{(-1)}$2.5	$^{(-5)}$4,041,000
	2	10.8	21.4		
	3	12.8	14.7		
29 May 2011	1	25.2	7.9	$^{(-3)}$4.5	$^{(-5)}$8,210,000
	2	17.2	8.5		
	3	15.6	9.5		
04 August 2011	1	6.4	2.3	$^{(-3)}$2.6	$^{(-5)}$70,203,000
07 September 2011	1	10.8	8.3		
	2	10.8	7.8		
	3	25.2	17.9		
18 October 2011	1	8.4	11.8	$^{(-3)}$12.0	$^{(-3)}$11,936,000
	2	15.2	14.7		
	3	14.4	22.7		
20 February 2012	1	5.6	9.8	$^{(-3)}$4.7	
	2	7.6	13.4		
	3	5.6	6.2		
15 March 2012	1	6.0	3.4	7.5	
	2	6.0	2.8		
	3	7.2	3.3		
08 July 2012	1	7.2	16.8	$^{(-3)}$63.9	$^{(-4)}$54,996,000
	2	11.2	20.2		
	3	12.8	19.7		
10 September 2012	2	12.4	20.4	$^{(-3)}$69.3	$^{(-5)}$200,907,000
	3	43.2	9.9		
12 December 2012	1	7.2	2.6	18.0	$^{(-2)}$21,495,000
	2	8.4	3.3		
	3	11.2	4.2		
08 January 2013	1	3.2	6.0		
	2	6.0	5.9		
	3	4.0	4.0		
21 February 2013	1	2.4	5.4	$^{(-3)}$1.5	
	2	2.4	5.6		
	3	2.8	4.6		
14 October 2013	1	9.6	14.8		
	2	10.0	5.8		
	3	17.6	1.6		
21 February 2014	1	2.4	1.2		
	2	3.6	2.4		
	3	8.8	1.6		

[a]A negative number in parenthesis indicates the number of days for which individual data were accumulated prior to each sampling date.

Inc., Chicago). The MLR models can be expressed as the following:

$$Y_i = a + b_j \times R_{\mathrm{rs}i,j} + \varepsilon_i \quad (3)$$

$$\varepsilon_i \sim N(0, \sigma^2)$$

where Y_i is the Chl-a or TSS concentrations of sample i ($i = 39$, the total number of images). a refers to the intercept, b_j is the slope of R_{rs} for the spectral band j ($j = 4$) in the i-th image, and ε_i indicates the random error term having its variance σ^2.

The MLR models were initially constructed using the satellite images in 2011–2012 and then evaluated with the data in 2013–2014, to examine their

Table 2
Rank order of important spectral wavelengths which are determined by the LH-OAT sensitivity analysis to develop different MLR models from the GOCI and MODIS image data[a]

	GOCI images				MODIS images			
Rank	MLR(G)-Chl-a	Sensitivity	MLR(G)-TSS	Sensitivity	MLR(M)-Chl-a	Sensitivity	MLR(M)-TSS	Sensitivity
1	B1 (412 nm)	13,908	B2 (443 nm)	2,185	B6 (547 nm)	1,195,608	B5 (531 nm)	3,948
2	B2 (443 nm)	1,896	B1 (412 nm)	1,845	B4 (488 nm)	167,219	B6 (547 nm)	1,664
3	B6 (680 nm)	466	B6 (680 nm)	661	B1 (412 nm)	125,292	B4 (488 nm)	1,073
4	B4 (555 nm)	448	B8 (865 nm)	365	B8 (645 nm)	67,455	B3 (469 nm)	224
5	B5 (660 nm)	445	B3 (490 nm)	169	B7 (555 nm)	46,890	B1 (412 nm)	121
6	B7 (745 nm)	122	B7 (745 nm)	66	B10 (678 nm)	35,088	B8 (645 nm)	121
7	B8 (865 nm)	98	B5 (660 nm)	10	B5 (531 nm)	18,755	B2 (443 nm)	113
8	B3 (490 nm)	56	B4 (555 nm)	2	B9 (667 nm)	17,761	B7 (555 nm)	89
9					B3 (469 nm)	5,423	B10 (678 nm)	23
10					B2 (443 nm)	3,918	B9 (667 nm)	5

[a]The MLR models which are developed individually based on the satellite images (GOCI: G and MODIS: M) and dependent variables (i.e. Chl-a and TSS) are abbreviated as MLR(G)-Chl-a, MLR(G)-TSS, MLR(M)-Chl-a, and MLR(M)-TSS. Note that the top four spectral wavelengths ranked high are only used as predictor variables in different MLR models.

applicability in local estuarine reservoirs, as discussed in Section 2.3. Their performance was also compared with the field water quality measurements with respect to the coefficient of determination (R^2) and root mean square error (RMSE).

2.5. Comparison of the performance of different models

The MLR models (i.e. MLR(G)-Chl-a, MLR(M)-Chl-a, MLR(G)-TSS, and MLR(M)-TSS) were compared with different types of bio-optical algorithms that mainly employed the band ratio (referred as the conventional models, see Table 3). The conventional models we used in this study included the OC4v.4 and OC3 M algorithms as well as the GDPS standard, and Clark's models. The OC4v.4 and OC3 M algorithms are the models specifically developed for prediction of the Chl-a levels using the SeaWiFS (a prototype of GOCI) and MODIS images, respectively. In contrast, their corresponding algorithms for the TSS estimation were the

Table 3
Bio-optical algorithms for estimating the Chl-a and TSS levels in surface waters implemented in the conventional (i.e. OC4v.4, OC3 M, GDPS standard, and Clark) models[a]

Types	Conventional models
OC4v.4	Chl-a = $10^{f_0+f_1\times R+f_2\times R^2+f_3\times R^3+f_4\times R^4}$ where $R=\max\left[\frac{R_{rs}(443)<R_{rs}(490)<R_{rs}(510)}{R_{rs}(555)}\right]$, $f_0=0.366$, $f_1=-3.067$, $f_2=1.930$, $f_3=0.649$, and $f_4=-1.532$
OC3 M	Chl-a = $10^{f_0+f_1\times R+f_2\times R^2+f_3\times R^3+f_4\times R^4}$ where $R=\max\left[\frac{R_{rs}(443)<R_{rs}(490)}{R_{rs}(555)}\right]$, $f_0=0.2424$, $f_1=-2.7423$, $f_2=1.8071$, $f_3=0.0015$, and $f_4=-1.2280$
GDPS standard	TSS = $945.07\times R^{1.137}$ where $R=R_{rs}(555)$
Clark	TSS = $10^{f_0+f_1\times R+f_2\times R^2+f_3\times R^3+f_4\times R^4+f_5\times R^5}$ where $R=\max\left[\frac{nLw(412)<nLw(443)}{R_{rs}(510)}\right]$, $f_0=0.850$, $f_1=-0.123$, $f_2=37.096$, $f_3=88.035$, $f_4=-30.594$, and $f_5=-48.004$

[a]Note that the coefficients for f_i represent the values that are optimized in individual models. nLw and λ indicate the normalized water-leaving radiance (estimated from the upwelling radiance) and wavelength in nm, respectively.

GDPS standard (with the GOCI data) and Clark's models (with the MODIS data). Note that unlike other algorithms, the GDPS standard model only uses a single band for prediction of the TSS levels. The two- or three-bands NIR-red algorithms fell into a category of the recent models in this study, which were designed for the Chl-a estimation (see Table 4). In addition, some recent bioalgorithms which were developed for turbid waters through single or multiple bands, including the band ratio, from the GOCI and MODIS images were used for comparison purposes with the MLR models for TSS.

A comparison was also made between the outputs of the MLR models and those of the CE-QUAL-W2 model. As a laterally averaged hydrodynamic and water quality model, the CE-QUAL-W2 model simulated the behavior of Chl-a and TSS in the YAR and was used to verify the usefulness of the MLR models in rapidly screening local estuarine water quality. Before running a simulation, topography data which were obtained from 140 sites in the YAR using an acoustic Doppler profiler (SonTek/Xylem Inc., California) were provided as inputs to the CE-QUAL-W2 model. Based on the bathymetry data, the YAR was eventually divided into 45 active segments and 26 vertical layers [36]. Once all necessary input data were provided, a pattern search technique was applied to determine the optimal values of kinetic and hydrodynamic parameters in the model (Table 5).

3. Results

3.1. Evaluation of constructed MLR models

When constructing the individual MLR models through the sensitivity analysis, slightly different wavelengths in two satellite images contributed to the Chl-a estimation in the YAR (see Table 2). For example, blue (412 and 443 nm), green (555 nm), and red bands (680 nm) were the most sensitive to the Chl-a estimation for the GOCI images, whereas blue (412 and 488 nm), green (547 nm), and red bands (645 nm) were considered more important for the MODIS data. The same applied to the TSS calculation in the YAR. In other words while blue (412 and 443 nm), red (680 nm), and NIR bands (865 nm) were the most sensitive to the TSS estimation in the GOCI images, the wavelengths in blue (488 and 469 nm) and green bands (531 and 547 nm) were selected as predictor variables for the MODIS data. Note that green (520–555 nm) and red (660 nm) bands are commonly chosen as the best variables for the TSS calculation in literature [27–31].

Base on the results above, red (680 and 645 nm), blue (412, 443, and 488 nm), and green bands (555 and 547 nm) were significantly correlated with the Chl-a levels and dominantly affected the optical properties at the surface layer of the YAR. These findings were somewhat consistent with the previous studies in that the absorption maxima and minimum for this

Table 4
Bio-optical algorithms for estimating the Chl-a and TSS levels in different area available in the recent studies using two satellite data (i.e. the GOCI and MODIS images)

Images	Wavelengths λ_1 (nm)	λ_2 (nm)	λ_3 (nm)	Bio-optical algorithms	Refs.
GOCI	412	443	490	$\text{Chl-a} = 1.8528 \times R^{-3.263}$ where $R = \left[\frac{R_{rs}(443)+R_{rs}(490)-R_{rs}(412)}{R_{rs}(555)}\right]$	[41]
GOCI	680	745		$\text{Chl-a} = 56.81 \times \left[R_{rs}^{-1}(\lambda_1) \times R_{rs}(\lambda_2)\right] - 32.64$	[20]
MODIS	667	748		$\text{Chl-a} = 10^{2.408+1.49\times\log 10\cdot[R_{rs}^{-1}(\lambda_1)\times R_{rs}(\lambda_2)]}$	[24]
MODIS	662–672	743–753		$\text{Chl-a} = -16.2 + 136.3 \times [R_{rs}^{-1}(\lambda_1) \times R_{rs}(\lambda_2)]$	[14]
MODIS	678	748		$\text{Chl-a} = 1.472 \times e^{6.3462\cdot[R_{rs}^{-1}(\lambda_1)\times R_{rs}(\lambda_2)]}$	[12]
GOCI	660			$\text{TSS} = 1.7532 \times e^{204.26\cdot(\lambda_1)}$	[31]
GOCI	490	745		$\text{TSS} = 10^{1.0758-1.123\cdot(\lambda_2/\lambda_1)}$	[33]
GOCI	660			$\text{TSS} = 1.545 \times e^{179.53\cdot(\lambda_1)}$	[28]
MODIS	620–670			$\text{TSS} = -1.91 \times 1140.25 \cdot (\lambda_1)$	[34]
MODIS	555	645	488	$\text{TSS} = 10^{0.6311+[22.2158\cdot(\lambda_1+\lambda_2)]-[0.5239\cdot(\lambda_1+\lambda_3)]}$	[30]
MODIS	645			$\text{TSS} = 2.49 \times e^{97.19\cdot(\lambda_1)}$	[32]

Table 5
Major model parameters (i.e. 21 kinetic and 5 hydraulic parameters) adjusted from the calibration process of the CE-QUAL-W2 model[a]

Constituents	Parameters	Definitions (units)	Min	Max	This study
Algae	AG	Algal growth rate (d^{-1})	0.2	0.3	0.25
	AR	Algal dark respiration rate (d^{-1})	0.005	0.2	0.00523
	AE	Algal excretion rate (d^{-1})	0.005	0.2	0.00523
	AM	Algal mortality rate (d^{-1})	0	0.1	0.001
	AS	Algal settling rate (m/d)	0	4.0	0.266
	AHSP	Algal half-saturation P limited growth (g/m^3)	0.0005	0.0800	0.0632
	AHSN	Algal half-saturation N limited growth (g/m^3)	0.001	0.400	0.003
	ASAT	Algal light saturation (W/m^2)	19	170	19
	AT1	Lower temperature for algal growth (℃)	5	10	6
	AT2	Lower temperature for maximum algal growth (℃)	15	30	26
	AT3	Upper temperature for maximum algal growth (℃)	20	40	21
	AT4	Upper temperature for algal growth (℃)	24	50	30
	ACHLA	Ratio between algal biomass and Chl-a	40	220	65
Organic matter	LDOMDK	Labile dissolved organic matter (DOM) decay rate (d^{-1})	0.010	0.64	0.014
	RDOMDK	Refractory DOM decay rate (d^{-1})	0.0001	0.0064	0.001
	LPOMDK	Labile particulate organic matter (POM) decay rate (d^{-1})	0.001	0.12	0.082
	POMS	POM settling rate (d^{-1})	0.020	2	0.020
Phosphorus	PO4R	Sediment release rate of P (d^{-1})	0.000	0.03	0.000
Ammonium	NH4R	Sediment release rate of N (d^{-1})	0.001	0.4	0.209
	NH4DK	Ammonium decay rate (d^{-1})	0.001	1.3	0.017
Nitrate	NO3DK	Nitrate decay rate (d^{-1})	0.030	0.15	0.029
Hydraulic parameters	AX	Horizontal eddy viscosity and diffusivity (m^2/s)	1*		1
	CBHE	Coefficient of bottom heat exchange ($W\ m^2/s$)	0.3*		0.5
	SRO	Fraction solar radiation absorbed at the water surface	0.6*		0.45
	WSCFN	Wind sheltering factor	0.1–0.5*		0.9
	FRICC	Chezy bottom friction factor (m^2/s)	0.3*		0.5

[a]The values marked with an asterisk (*) are obtained from two reference sources [36,51].

constituent were usually detected at approximately 440 and 550 nm, and thereby those bands were typically used to estimate the Chl-a levels [15–18]. However, note that the band ratio method with blue and green wavelengths is no longer used to estimate the Chl-a concentrations in turbid waters. Interestingly, inclusion of the wavelengths in red bands resulted in an improvement in the prediction accuracy of two MLR models, MLR(G)-Chl-a and MLR(M)-Chl-a, in our study (data not shown).

In the case of the TSS estimation, the selected bands in the GOCI images were widely distributed in the visible and NIR wavelengths (412 nm > 443 nm > 680 nm > 865 nm). These results were also consistent with the previous studies for CASE-2 water which used NIR and red wavelengths ranging between 660 and 865 nm as optimal wavelengths [27,31–33]. Conversely, the selected bands in the MODIS data were intensively distributed on the blue and green wavelengths (440–555 nm) which maximally absorbed the TSS concentrations in open oceans. Thus, the MLR(M)-TSS appears to closely resemble the conventional models for TSS.

The four wavelengths selected according to the satellite types and dependent variables were used to construct different MLR models (i.e. MLR(G)-Chl-a, MLR(M)-Chl-a, MLR(G)-TSS, and MLR(M)-TSS) using the enter method that only allowed them to be included as predictor variables. The constructed MLR models were initially tested with the data-set of the GOCI and MODIS images for 2011–2012 and re-assessed with the other data-set for 2013–2014 (Table 6). From the initial test, the coefficients of individual variables in each MLR model were determined along with their t statistic values (data not shown). The t statistic showed that the significance of the wavelength in 469 nm at MLR(M)-TSS was only greater than 0.05, indicating this particular variable should be carefully reinvestigated and included in the model refined in the future. Despite this shortcoming,

Table 6
Comparing the performance between the MLR and conventional models in two data-sets, one for 2011–2012 and the other for 2013–2014, which are constructed from the GOCI and MODIS image data[a]

		R^2 (RMSE)							
		MLR models				Conventional models			
		Chl-a		TSS		Chl-a		TSS	
Data-sets	Sites	MLR(G)-Chl-a	MLR(M)-Chl-a	MLR(G)-TSS	MLR(M)-TSS	OC4v.4	OC3 M	GDPS standard	Clark
2011–2012	Site 1	0.49 (3.71)	0.80 (2.60)	0.01 (4.12)	0.75 (3.24)	0.24 (6.36)	0.11 (8.29)	0.09 (7.89)	0.00 (4.19)
	Site 2	0.71 (5.06)	0.63 (4.71)	0.71 (3.39)	0.77 (2.62)	0.34 (6.87)	0.71 (6.54)	0.75 (1.92)	0.35 (7.23)
	Site 3	0.29 (5.72)	0.61 (4.64)	0.89 (3.07)	0.74 (2.63)	0.76 (4.91)	0.33 (7.24)	0.72 (3.83)	0.34 (6.85)
2013–2014	Site 1	0.56 (4.18)	0.62 (3.21)	0.74 (4.66)	0.49 (2.22)	0.88 (4.10)	0.77 (8.30)	0.64 (5.33)	0.44 (6.99)
	Site 2	0.80 (3.56)	0.76 (2.17)	0.88 (3.43)	0.66 (3.77)	0.67 (5.59)	0.37 (8.740)	0.79 (4.41)	0.15 (10.53)
	Site 3	0.66 (3.20)	0.98 (1.71)	0.98 (0.84)	0.66 (3.53)	0.60 (5.15)	0.05 (7.54)	0.77 (3.09)	0.21 (7.20)

[a]Abbreviations: R^2 = the coefficient of determination and RMSE = the root mean square error.

we simply included the wavelength in 469 nm for MLR(M)-TSS to maintain consistency in the MLR models in this preliminary study. The constructed MLR models generally showed moderate to strong moderate agreement with the observed data for both 2011–2012 and 2013–2014, except for site 1 in MLR(G)-TSS and site 3 in MLR(G)-TSS. On average, the MLR models developed from MODIS data appeared to be more accurate than those of GOCI data in terms of R^2 and RMSE, except for MLR(G)-TSS. Although we cannot explain the exact reason for the low accuracy for a few sites and difference in performance between the MLR models, all these results demonstrate that they are still useful tools for estimating the Chl-a and TSS levels in local waters.

3.2. Comparison of the performance between MLR models and different bio-optical algorithms

When the performance of the MLR models was compared against the conventional models which were developed from the GOCI and MODIS images, their estimation accuracy for both Chl-a and TSS seemed to be more accurate than the conventional models on average (see Table 6). This is probably because the disturbance of the optical properties in local turbid waters is not accounted for in the conventional models [17,28]. In the case of the Chl-a estimation, the OC4v.4 model was generally more accurate than the OC3 M model. For the TSS estimation, the GDPS standard showed more powerful performance than the Clark's model. Surprisingly, the estimation accuracy of the conventional models for both Chl-a and TSS in the initial data-set was always low in site 1, as shown in MLR(G)-TSS. Although we did not clearly explain their poor performance, this was not simply caused by geographical features of the monitoring site. This is because the estimation accuracy of the conventional models is still high in the other data-set for 2013–2014 as well as for other MLR models in any of the two data-sets, except for MLR(G)-TSS.

A comparison was also made between the MLR models of Chl-a and TSS and other bio-optical algorithms that used the specific wavelengths in the GOCI and MODIS images (see Table 4 and Fig. 2). From the figure, it was found that the MLR models showed better performance than other models available in the recent studies, except for MLR(M)-Chl-a (Fig. 2(c)). This result clearly indicate that site-specific models are more suitable for assessing local water conditions than almost any other model as long as the wavelengths from the satellite images are carefully selected in the models and strictly examined in multiple data-sets. Also, as the resolution of satellite images may affect model performance, this issue is clearly addressed in future comparison studies.

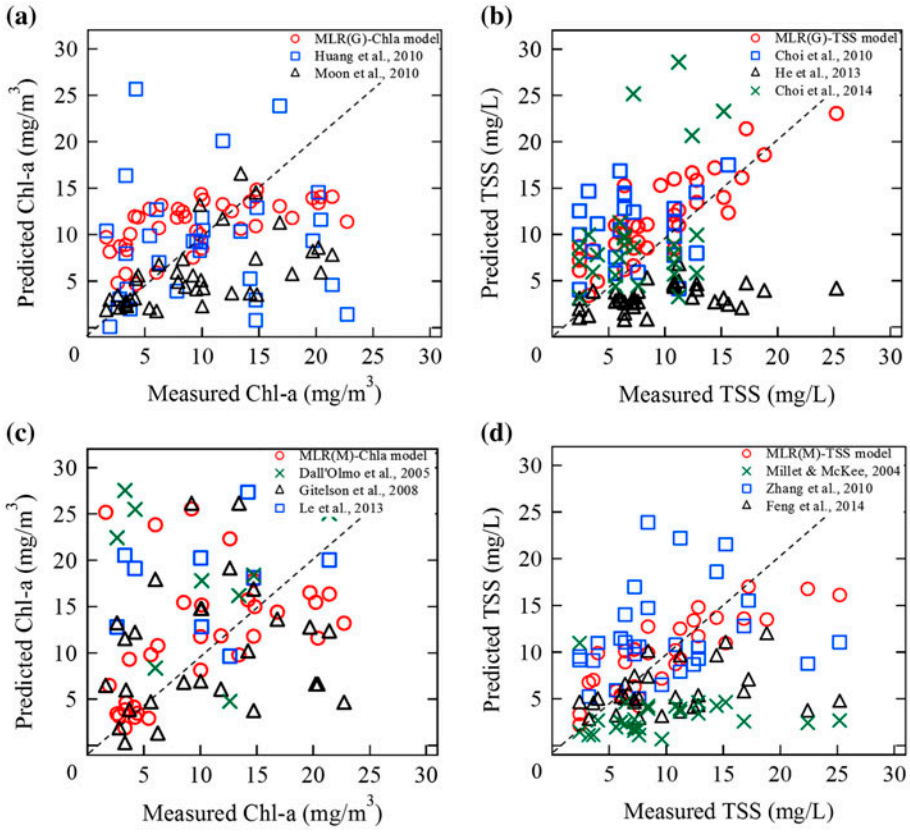

Fig. 2. Comparing the performance between the MLR models of Chl-a and TSS, (a) MLR(G)-Chl-a, (b) MLR(G)-TSS, (c) MLR(M)-Chl-a, and (d) MLR(M)-TSS, and other bio-optical algorithms available in the recent studies.

3.3. *Comparison of the performance between MLR models and CE-QUAL-W2*

After setting appropriate initial and boundary conditions (e.g. precipitation and inflow), the CE-QUAL-W2 model which was adjusted by the pattern search technique predicted the water elevation in the YAR successfully ($R^2 = 0.81$, data not shown). Fig. 3 shows the predicted and observed water quality profiles on a monthly basis at the water surface in three monitoring sites of the YAR over two years, 2011–2012. As shown in the figure, the prediction accuracy for water temperature was the highest among all parameters (Fig. 3(d)–(f)), which was followed by DO (Fig. 3(a)–(c)). The simulation results for T-N were also in good agreement with the observed data for three monitoring sites of the YAR, even though some differences were observed between them mainly at the beginning and end of the simulation (Fig. 3(g)–(i)). In fact, the T-N concentrations in the reservoir were high in late winter and early spring, and then decreased during the summer season due to largely the dilution effect from heavy rainfall and high water inflow as well as uptake by algae, to a less extent [48]. Nutrient inputs from the interconnected reservoirs or surrounding agriculture area were not responsible for this deviation, as the concentrations of ammonia and nitrate were not underestimated in the model (data not shown).

Interestingly, the model appeared to constantly overestimate the T-P concentrations at three monitoring sites in the YAR (Fig. 3(j)–(l)), whereas the Chl-a and TSS levels were underestimated (Fig. 3(m)–(r)). There are two potential reasons for the overestimation of the T-P concentrations in the reservoir. First, the adsorption and precipitation processes of particulate phosphorus into the sediment could not be reflected in our model properly. For example, the adsorption process of ortho-P (PO_4) onto dissolved divalent metal cations such as Fe^{2+} and Mn^{2+}, which was responsible for the decrease of the T-P levels in the water columns [49], was not considered significantly in our simulation scenario. The second reason was related to the incorrect model input regarding the external phosphorus loading from upstream tributary [36,50]. The sewage treatment facilities constructed recently in the

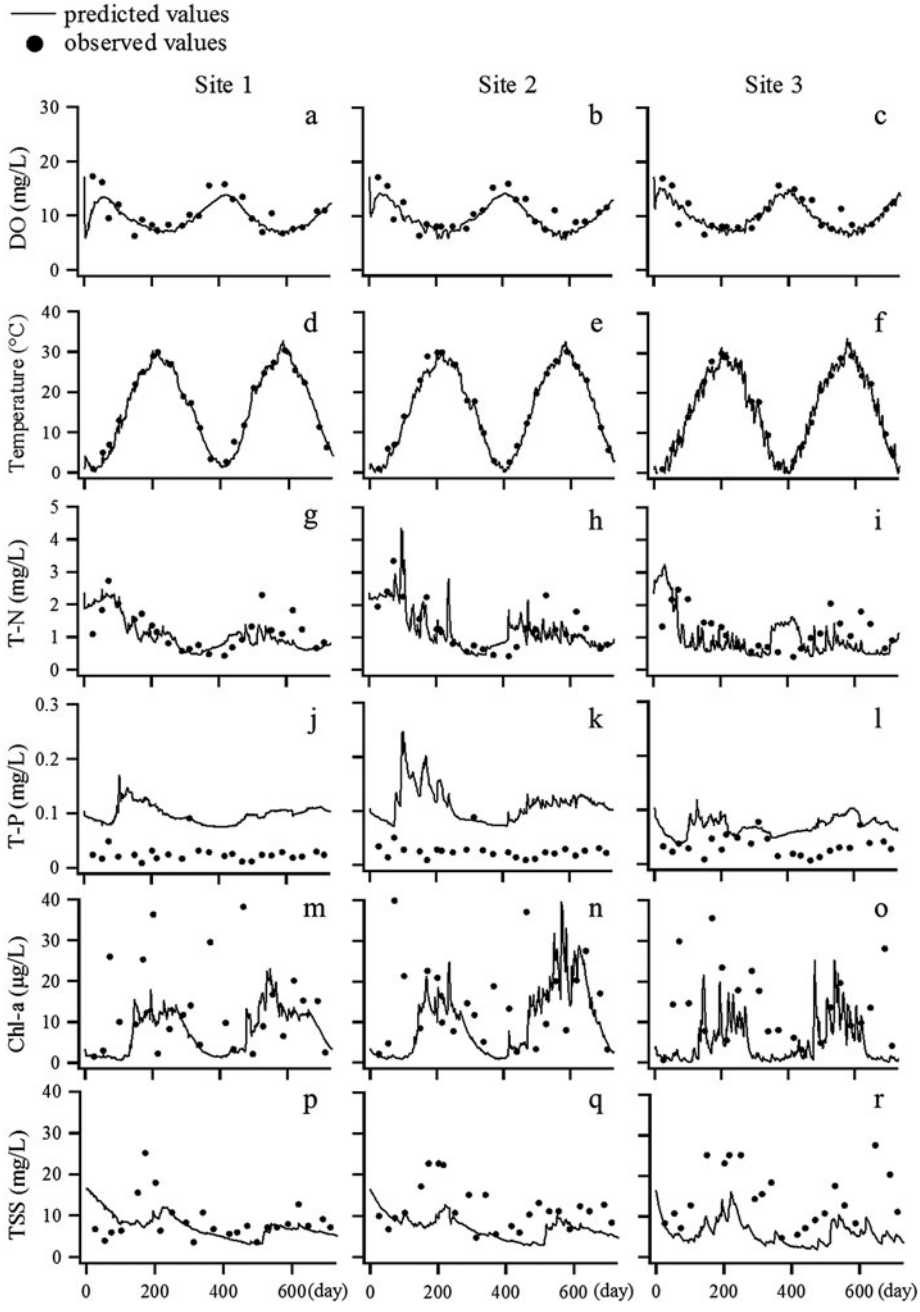

Fig. 3. Comparing monthly profiles of several key parameters, (a) through (c) for DO, (d) through (f) for temperature, (g) through (i) for T-N, (j) through (l) for T-P, (m) through (o) for Chl-a, and (p) through (r) for TSS, between field measurements and simulation results from the CE-QUAL-W2 model at water surface in three monitoring sites for the YAR during 2011–2012.

upstream of the YAR lowered the T-P loading to the reservoir [36]. However, this was not addressed accurately in our simulation due to a lack of actual flow and load data from the facilities.

There is some inherent difficulty when comparing the results of the MLR models and their corresponding simulation results from the CE-QUAL-W2 model due to a large difference between algorithms in estimating the Chl-a and TSS levels (Fig. 4). As discussed above, the prediction accuracy for Chl-a and TSS was unsatisfactory in the YAR (see Fig. 3), where large seasonal and spatial variations in the Chl-a and TSS concentrations were not sufficiently captured by the model. This was partially attributed to the inaccurate simulation of water quality constituents such as T-P and T-N which were associated with the dynamics of Chl-a and TSS

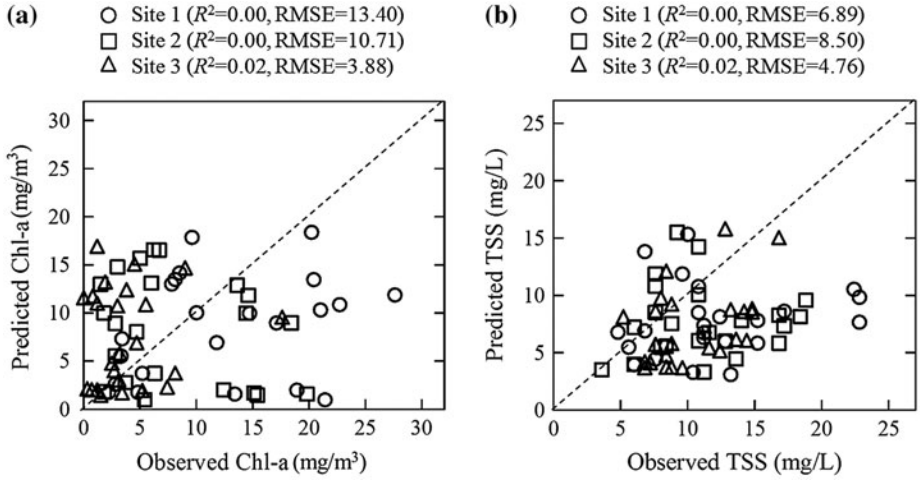

Fig. 4. Comparing the estimation accuracy between the MLR models and their corresponding results from the CE-QUAL-W2 model for (a) Chl-a and (b) TSS in the initial data-set during 2011–2012.

(e.g. zero order decay and algal growth) [36,50]. Accordingly, the deviation of the T-N and T-P predictions from the observed values appeared to be propagated into the Chl-a and TSS predictions in the model. Also, the governing equations in the CE-QUAL-W2 model were designed to simulate the laterally averaged velocity and water quality profiles. Thus, a lack of vertical transportation equations in the model is another potential reason for inadequate description of the Chl-a and TSS profiles in the reservoir [51,52]. Overall, all these results reveal that the MLR models developed from satellite observations are more useful in rapidly assessing surface water quality conditions than general water quality models, if adequate input data and description of transport mechanisms for the target reservoir are not addressed fully in the simulation models. Also, the results derived from the MLR models may be used to improve the accuracy of deterministic models, specifically when the environmental monitoring data are sparse.

4. Conclusion

The main objective of this study was to develop the MLR models from the GOCI and MODIS images to rapidly screen water quality conditions in the YAR. The following are the main outcomes in this study.

(1) Specific wavelengths in blue and green bands contributed to the Chl-a estimation, as shown in the previous studies. Including particular red and NIR wavelengths in the MLR models could additionally improve the accuracy of the Chl-a and TSS estimates, respectively. The constructed MLR models still showed good performance in the other data-set for 2013–2014.
(2) The MLR models were compared to the classical and recent bio-optical algorithms. The MLR models developed locally reflected site-specific water quality conditions better than any other models tested. There was an exception in one monitoring site presenting poor performance, but this was not clearly addressed in this study.
(3) The CE-QUAL-W2 model did not correctly capture the behavior of T-N and T-P in the YAR, whereas the simulation results for some parameters after the calibration process are satisfactory. This seemed to affect the performance of the Chl-a and TSS predictions in the model, revealing the usefulness of the MLR models in assessing local estuarine water quality. Once verified successfully, the outputs from the MLR models are, in turn, expected to enhance the input data quality for the general water quality models.

Acknowledgments

This research was supported by the Korea Ministry of Environment as "The Eco-innovation Project: Non-point source pollution control research group" and the National Research Foundation of Korea.

References

[1] H.W. Paerl, J. Huisman, Blooms like it hot, Science 320 (2008), 57–58.

[2] Y. Cha, S.S. Park, K. Kim, M. Byeon, C.A. Stow, Probabilistic prediction of cyanobacteria abundance in a Korean reservoir using a Bayesian Poisson model, Water Resour. Res. 50 (2014) 2518–2532.

[3] D.J. Conley, H.W. Paerl, R.W. Howarth, D.F. Boesch, S.P. Seitzinger, K.E. Havens, C. Lancelot, G.E. Likens, Controlling eutrophication: Nitrogen and phosphorus, Science 323 (2009) 1014–1015.

[4] V.H. Smith, S.B. Joye, R.W. Howarth, Eutrophication of freshwater and marine ecosystems, Limnol. Oceanogr. 51 (2006) 351–355.

[5] M.F. Coveney, E.F. Lowe, L.E. Battoe, E.R. Marzolf, R. Conrow, Response of a eutrophic, shallow subtropical lake to reduced nutrient loading, Freshwater Biol. 50 (2005) 1718–1730.

[6] D.R. de Figueiredo, A.S.S.P. Reboleira, S.C. Antunes, N. Abrantes, U. Azeiteiro, F. Gonçalves, M.J. Pereira, The effect of environmental parameters and cyanobacterial blooms on phytoplankton dynamics of a Portuguese temperate lake, Hydrobiologia 568 (2006) 145–157.

[7] Y. Park, K.H. Cho, J. Park, S.M. Cha, J.H. Kim, Development of early-warning protocol for predicting chlorophyll-a concentration using machine learning models in freshwater and estuarine reservoirs, Korea, Sci. Total Environ. 502 (2015) 31–41, doi: 10.1016/j.scitotenv.2014.09.005.

[8] H. Chang, Spatial analysis of water quality trends in the Han River basin, South Korea, Water Res. 42 (2008) 3285–3304, doi: 10.1016/j.watres.2008.04.006.

[9] H.R. Gordon, O.B. Brown, R.H. Evans, J.W. Brown, R.C. Smith, K.S. Baker, D.K. Clark, A semianalytic radiance model of ocean color, J. Geophys. Res. 93(D9) (1988) 10909–10924, doi: 10.1029/JD093iD09p10909.

[10] Y. Ahn, J. Moon, S. Gallegos, Development of suspended particulate matter algorithms for ocean color remote sensing, Korean J. Remote Sens. 17 (2001) 285–295.

[11] A. Morel, B. Gentili, Diffuse reflectance of oceanic waters. III. Implication of bidirectionality for the remote-sensing problem, Appl. Opt. 35 (1996) 4850–4862.

[12] C. Le, C. Hu, J. Cannizzaro, D. English, F. Muller-Karger, Z. Lee, Evaluation of chlorophyll-a remote sensing algorithms for an optically complex estuary, Remote Sens. Environ. 129 (2013) 75–89, doi: 10.1016/j.rse.2012.11.001.

[13] S. Maritorena, D.A. Siegel, A.R. Peterson, Optimization of a semianalytical ocean color model for global-scale applications, Appl. Opt. 41 (2002) 2705–2714, doi: 10.1364/AO.41.002705.

[14] A.A. Gitelson, G. Dall'Olmo, W. Moses, D.C. Rundquist, T. Barrow, T.R. Fisher, A simple semi-analytical model for remote estimation of chlorophyll-a in turbid waters: Validation, Remote Sens. Environ. 112 (2008) 3582–3593, doi: 10.1016/j.rse.2008.04.015.

[15] A. Morel, B. Gentili, A simple band ratio technique to quantify the colored dissolved and detrital organic material from ocean color remotely sensed data, Remote Sens. Environ. 113 (2009) 998–1011.

[16] J.E. O'Reilly, S. Maritorena, B.G. Mitchell, D.A. Siegel, K.L. Carder, S.A. Garver, Ocean color chlorophyll algorithms for SeaWiFS, J. Geophys. Res. 103(C11) (1998) 24937–24953.

[17] A.A. Gitelson, D. Gurlin, W.J. Moses, T. Barrow, A bio-optical algorithm for the remote estimation of the chlorophyll-a concentration in case 2 waters, Environ. Res. Lett. 4 (2009) 045003, doi: 10.1088/1748-9326/4/4/045003.

[18] A. Morel, L. Prieur, Analysis of variations in ocean color, Limnol. Oceanogr. 22 (1977) 709–722.

[19] K.L. Carder, F.R. Chen, J.P. Cannizzaro, J.W. Campbell, B.G. Mitchell, Performance of the MODIS semi-analytical ocean color algorithm for chlorophyll-a, Adv. Space Res. 33 (2004) 1152–1159.

[20] C. Huang, J. Zou, Y. Li, H. Yang, K. Shi, J. Li, Assessment of NIR-red algorithms for observation of chlorophyll-a in highly turbid inland waters in China, ISPRS J. Photogramm. Remote Sens. 93 (2014) 29–39, doi: 10.1016/j.isprsjprs.2014.03.012.

[21] L. Han, D.C. Rundquist, Comparison of NIR/RED ratio and first derivative of reflectance in estimating algal-chlorophyll concentration: A case study in a turbid reservoir, Remote Sens. Environ. 62 (1997) 253–261.

[22] Y.Z. Yacobi, W.J. Moses, S. Kaganovsky, B. Sulimani, B.C. Leavitt, A.A. Gitelson, NIR-red reflectance-based algorithms for chlorophyll-a estimation in mesotrophic inland and coastal waters: Lake Kinneret case study, Water Res. 45 (2011) 2428–2436.

[23] G. Dall'Olmo, A.A. Gitelson, D.C. Rundquist, Towards a unified approach for remote estimation of chlorophyll-a in both terrestrial vegetation and turbid productive waters, Geophys. Res. Lett. 30 (2003) HLS 1-1–1-4, doi: 10.1029/2003GL018065.

[24] G. Dall'Olmo, A.A. Gitelson, Effect of bio-optical parameter variability on the remote estimation of chlorophyll-a concentration in turbid productive waters: Experimental results, Appl. Opt. 44 (2005) 412–422, doi: 10.1364/AO.44.000412.

[25] D. Clark, E. Baker, A. Strong, Upwelled spectral radiance distribution in relation to particulate matter in sea water, Boundary-Layer Meteorol. 18 (1980) 287–298, doi: 10.1007/BF00122025.

[26] E. Siswanto, J. Tang, H. Yamaguchi, Y.-H. Ahn, J. Ishizaka, S. Yoo, Empirical ocean-color algorithms to retrieve chlorophyll-a, total suspended matter, and colored dissolved organic matter absorption coefficient in the Yellow and East China Seas, J. Oceanogr. 67 (2011) 627–650, doi: 10.1007/s10872-011-0062-z.

[27] S. Tassan, Local algorithms using SeaWiFS data for the retrieval of phytoplankton, pigments, suspended sediment, and yellow substance in coastal waters, Appl. Opt. 33 (1994) 2369–2378.

[28] J.-K. Choi, Y.-J. Park, B.R. Lee, J. Eom, J.-E. Moon, J.-H. Ryu, Application of the Geostationary Ocean Color Imager (GOCI) to mapping the temporal dynamics of coastal water turbidity, Remote Sens. Environ. 146 (2014) 24–35, doi: 10.1016/j.rse.2013.05.032.

[29] D. Doxaran, J.-M. Froidefond, P. Castaing, A reflectance band ratio used to estimate suspended matter concentrations in sediment-dominated coastal waters, Int. J. Remote Sens. 23 (2002) 5079–5085.

[30] M. Zhang, J. Tang, Q. Dong, Q. Song, J. Ding, Retrieval of total suspended matter concentration in the Yellow and East China Seas from MODIS imagery, Remote Sens. Environ. 114 (2010) 392–403.
[31] J. Choi, Y.-J. Park, J.-H. Ahn, H. Lim, J. Eom, J.-H. Ryu, GOCI, the world's first geostationary ocean color observation satellite, for the monitoring of temporal variability in coastal water turbidity, J. Geophys. Res. 117(C9) (2012) C09004, doi: 10.1029/2012JC008046.
[32] L. Feng, C. Hu, X. Chen, Q. Song, Influence of the Three Gorges Dam on total suspended matters in the Yangtze Estuary and its adjacent coastal waters: Observations from MODIS, Remote Sens. Environ. 140 (2014) 779–788, doi: 10.1016/j.rse.2013.10.002.
[33] X. He, Y. Bai, D. Pan, N. Huang, X. Dong, J. Chen, Using geostationary satellite ocean color data to map the diurnal dynamics of suspended particulate matter in coastal waters, Remote Sens. Environ. 133 (2013) 225–239, doi: 10.1016/j.rse.2013.01.023.
[34] R.L. Miller, B.A. McKee, Using MODIS Terra 250 m imagery to map concentrations of total suspended matter in coastal waters, Remote Sens. Environ. 93 (2004) 259–266, doi: 10.1016/j.rse.2004.07.012.
[35] Y.G. Lee, K.-G. An, P.T. Ha, K.-Y. Lee, J.-H. Kang, S.M. Cha, Decadal and seasonal scale changes of an artificial lake environment after blocking tidal flows in the Yeongsan Estuary region, Korea, Sci. Total Environ. 407 (2009) 6063–6072, doi: 10.1016/j.scitotenv.2009.08.031.
[36] Y. Park, K.H. Cho, J.-H. Kang, S.W. Lee, J.H. Kim, Developing a flow control strategy to reduce nutrient load in a reclaimed multi-reservoir system using a 2D hydrodynamic and water quality model, Sci. Total Environ. 466–467 (2014) 871–880, doi: 10.1016/j.scitotenv.2013.07.041.
[37] R.E. Carlson, J. Simpson, A Coordinator's Guide to Volunteer Lake Monitoring Methods, North American Lake Management Society, Madison, WI, 1996.
[38] X. He, D. Pan, Y. Bai, D. Wang, Z. Hao, A new simple concept for ocean colour remote sensing using parallel polarisation radiance, Sci. Rep. 4 (2014) 3748, doi: 10.1038/srep03748.
[39] K.G. Ruddick, F. Ovidio, M. Rijkeboer, Atmospheric correction of SeaWiFS imagery for turbid coastal and inland waters, Appl. Opt. 39 (2000) 897–912, doi: 10.1364/AO.39.000897.
[40] B.R. Lee, J.H. Ahn, Y.-J. Park, S.-W. Kim, Turbid water atmospheric correction for GOCI: Modification of MUMM algorithm, Korean J. Remote Sens. 29 (2013) 173–182.
[41] J.-E. Moon, Y.-J. Park, J.-H. Ryu, J.-K. Choi, J.-H. Ahn, J.-E. Min, Initial validation of GOCI water products against in situ data collected around Korean peninsula for 2010–2011, Ocean Sci. J. 47 (2012) 261–277.
[42] B. Nechad, De V. Cauwer, Y. Park, K.G. Ruddick, Suspended Particulate Matter (SPM) mapping from MERIS imagery. Calibration of a regional algorithm for the Belgian coastal waters, Proceedings of the MERIS User Workshop, November 10–13, Frascati, 2003. Available from: <http://envisat.esa.int/workshops/meris03/participants/139/paper_19_nechad.pdf>.
[43] C. Hu, K.L. Carder, F.E. Muller-Karger, How precise are SeaWiFS ocean color estimates? Implications of digitization-noise errors, Remote Sens. Environ. 76 (2001) 239–249, doi: 10.1016/S0034-4257(00)00206-6.
[44] R.L. Iman, W.J. Conover, Small sample sensitivity analysis techniques for computer models.with an application to risk assessment, Commun. Statistics-theory Methods 9 (1980) 1749–1842, doi: 10.1080/03610928008827996.
[45] A. van Griensven, T. Meixner, A global and efficient multi-objective auto-calibration and uncertainty estimation method for water quality catchment models, J. Hydroinf. 9 (2007) 277–291.
[46] D.R. Legates, G.J. McCabe, Evaluating the use of "goodness-of-fit" Measures in hydrologic and hydroclimatic model validation, Water Resour. Res. 35 (1999) 233–241.
[47] K. Holvoet, A. van Griensven, P. Seuntjens, P.A. Vanrolleghem, Sensitivity analysis for hydrology and pesticide supply towards the river in SWAT, Phys. Chem. Earth Parts A/B/C 30 (2005) 518–526
[48] K.H. Cho, J.-H. Kang, S.J. Ki, Y. Park, S.M. Cha, J.H. Kim, Determination of the optimal parameters in regression models for the prediction of chlorophyll-a: A case study of the Yeongsan Reservoir, Korea, Sci. Total Environ. 407 (2009) 2536–2545, doi: 10.1016/j.scitotenv.2009.01.017.
[49] H.S. Lee, S.W. Chung, J.K. Choi, B.H. Min, Feasibility of curtain weir installation for water quality management in Daecheong Reservoir, Desalin. Water Treat. 19 (2010) 164–172.
[50] D.-K. Kim, W. Zhang, S. Watson, G.B. Arhonditsis, A commentary on the modelling of the causal linkages among nutrient loading, harmful algal blooms, and hypoxia patterns in Lake Erie, J. Great Lakes Res. 40 (2014) 117–129.
[51] T.E. Coles, S.A. Wells, CE-QUAL-W2: A Two-dimensional Laterally Averaged, Hydrodynamic and Water Quality Model, Version 3.1. Instruction Report EL-03-1, US Army Engineering and Research Development Center, Vicksburg, MS, 2003.
[52] T.M. Cole, E.M. Buchak, CE-QUAL-W2: A Two-Dimensional, Laterally Averaged, Hydrodynamic and Water Quality Model, Version 2.0. User Manual, DTIC Document, 1995.